03 Aug 2005

Multicomponent Flow-Transport-Reaction Modeling of Trickle Bed Reactors: Application to Unsteady State Liquid Flow Modulation

M. R. Khadilkar

M. (Muthanna) H. Al-Dahhan
Missouri University of Science and Technology, aldahhanm@mst.edu

M. P. Duduković

Recommended Citation

M. R. Khadilkar et al., "Multicomponent Flow-Transport-Reaction Modeling of Trickle Bed Reactors: Application to Unsteady State Liquid Flow Modulation," *Industrial and Engineering Chemistry Research*, vol. 44, no. 16, pp. 6354 - 6370, American Chemical Society, Aug 2005.
The definitive version is available at https://doi.org/10.1021/ie0402261

Multicomponent Flow-Transport-Reaction Modeling of Trickle Bed Reactors: Application to Unsteady State Liquid Flow Modulation

M. R. Khadilkar,† M. H. Al-Dahhan, and M. P. Duduković*

Chemical Reaction Engineering Laboratory, Department of Chemical Engineering, Campus Box 1198, Washington University, St. Louis, Missouri 63130

A one-dimensional reactor and catalyst pellet scale flow-transport-reaction model utilizing the multicomponent Stefan−Maxwell formulation for inter- and intraphase transport is developed to simulate unsteady state operation in trickle bed reactors. The governing equations and method of solution are discussed. Results are presented for a model reaction system (hydrogenation of α-methylstyrene) under gas reactant limiting conditions, for liquid flow modulation as a test case of unsteady state operation. Model simulations predict that periodic liquid flow modulation can alter the supply of liquid and gaseous reactants to the catalyst and result in reactor performance enhancement above that achieved in steady state operation. The effects of key modulation parameters such as the total cycle period, cycle split, and liquid mass velocity are simulated, and model predictions are found to be in agreement with experimentally observed trends in the literature.

Introduction

Trickle bed reactors are three phase reactors with the solid phase in the form of a packed catalyst bed and liquid and gas flowing concurrently downward through the interstitial space. These reactors are used extensively for hydrotreating and hydrodesulfurization applications in the refining industry, and also for hydrogenation, oxidation, and hydrodenitrogenation applications in the chemical, biochemical, and environmental remediation industry.[1−3] Although trickle bed reactors have traditionally been operated under steady state conditions, recent experimental studies have explored unsteady state operation[4−11] and demonstrated the possibility of performance enhancement in laboratory reactors. The potential for performance enhancement arises from the competition between the gas and liquid phases in supplying reactants to the catalyst as well as the complex interaction between fluid dynamics, catalyst wetting, and reaction. This potential for improved performance in transient operation has been utilized successfully in other multiphase reactors, adsorbers, ion exchangers, etc., on industrial scale,[4] but has not been implemented on industrial trickle bed reactors.

The literature on unsteady state behavior in chemical systems was reviewed by Silveston[4] and classified into two categories: (i) parameter forcing and (ii) flow reversal. Most of the investigations summarized in his review were parameter forcing studies on stirred tanks, heat exchangers, ion exchangers, and some flow reversal studies in gas−solid fixed beds, adsorbers, and fractionators. On the basis of the observations of these systems, several strategies were suggested for possible performance enhancement in trickle bed reactors,[4] such as modulation of (i) flow, (ii) composition, or (iii) catalyst activity. Some of these have been considered in the few experimental studies reported in literature.[5−8,10−16] The test reaction systems and operating conditions of these studies are summarized in Table 1. These studies focus on flow and activity modulation with cycle times ranging from a few minutes to as high as 80 min and performance enhancement ranging from a few percent to almost 400%. A few modeling studies have appeared in the literature, dealing with both transient and pseudotransient models.[5,10,11,16−23] The key features and test reaction systems utilized in these studies are summarized in Table 2. These models are primarily an extension of the steady state approach and have the following shortcomings, which prevent them from being applied to real unsteady state or periodic systems:

(i) Most models are based on the plug flow assumption or straightforward extensions and do not consider the change in phase velocity and holdup with spatial and temporal coordinates.

(ii) Many models rely on the assumption of equilibrium between phases and some even use the pseudohomogeneous approach to simplify computation of the solution.

(iii) The models assume pseudotransient behavior and do not account for true accumulation terms for nonlimiting species.

(iv) Single component mass transfer terms are considered with coefficients calculated from low flux, dilute solution, thermodynamically ideal fluid conditions.

(v) Spatial terms on the catalyst level are dropped in some variations of the models to simplify computation.

(vi) Reaction and transport of only the limiting species is considered by keeping other concentrations invariant.

(vii) Multicomponent transport between phases has not been considered in most models, and hence the net mass and energy transport across the interface such as evaporation and condensation is not accounted for.

This study focuses on the development of an unsteady state periodic operation model based on multiphase flow, multicomponent transport, and reaction under unsteady state conditions to explain the phenomena reported in the recent experimental studies. The developed model is considered as a step in the direction of eliminating some of the above-mentioned simplifications. In this work, the model is applied to a particular case of

* To whom correspondence should be addressed.
† Present address: GE Plastics, One Lexan Lane, Mt. Vernon, IN 47620.

10.1021/ie0402261 CCC: $30.25
Published on Web 03/03/2005

Table 1. Reported Experimental Studies of Unsteady State Operation in Trickle Beds

author(s)	system studied	modulation strategy	L and G flow rates	cycle period (τ) and split (σ)	performance enhancement (%) (temp rise, °C)
Haure et al.[5]	SO_2 oxidation	flow (non-isothermal)	$U_L = 0.03-1.75$ mm/s $U_G = 1-2$ cm/s	$\tau = 10-80$ min ($\sigma = 0.1$, 0−0.5)	30−50%
Lange et al.[6]	cyclohexene hydrogenation	composition (non-isothermal)	$Q_L = 80-250$ mL/h conc = 5−100%	$\tau = 4-30$ min ($\sigma = 0.2-0.5$)	2−15% (temp rise = 30 °C)
	α-methylstyrene hydrogenation	liquid flow (isothermal)	$Q_L = 0-300$ mL/h, $Q_G = 20$ L/h	$\tau = 1-10$ min ($\sigma = 0.25-0.5$)	
Lee et al.[8]	SO_2 oxidation	adiabatic flow modulation	$U_L = 0.085-0.212$ cm/s, $SU_G = 1000$ h^{-1}	$\tau =$ up to 60 min ($\sigma = 0.02-0.1$)	
Castellari and Haure[7]	α-methylstyrene hydrogenation	non-isothermal	$Q_L = 2.27$ mL/s $Q_G = 900$ mL/s	$\tau = 5-45$ min ($\sigma = 0.3-0.5$)	400% (temp rise = 45 °C)
Khadilkar et al.[10,11,48]	α-methylstyrene hydrogenation	flow modulation	$Q_L = 2.27$ mL/s $Q_G = 900$ mL/s	$\tau = 0.5-10$ min ($\sigma = 0.1-0.66$)	5−50% (temp rise = 6 °C)

Table 2. Reported Unsteady State Models for Trickle Bed Reactors

authors	model features	reaction system	remarks
Yan[17]	plug flow, gas−liquid equilibrium, apparent rate on catalyst	hydrocracking	temp profiles with and without quenching predicted
Haure et al.[5]	non-isothermal plug flow model with liquid ON−OFF, mass transfer controlling the rate	SO_2 oxidation	thermal waves and temp rise compared with experimental observations
Stegasov et al.[18]	non-isothermal plug flow with liquid ON−OFF, mass transfer control	SO_2 oxidation	temp and concentration profiles predicted
Wu et al.[19]	local transient model with multiple reaction, mass transfer variation with high frequency	three model systems of multiple series and parallel reactions	rate enhancement with varying frequency examined for natural pulsing
Warna and Salmi[20]	parabolic PDEs for gas and liquid phases, pseudo transient simulation to steady state	toluene hydrogenation, SO_2 oxidation	reactor dynamics from start-up to steady state studied
Yamada and Goto[21]	plug flow with parameter optimization	hydrogenation to amino acid	optimal cycle period for product removal and catalyst regeneration calculated
Gabarain et al.[22]	three zone model, completely wetted, externally dry and internally dry pellets	hydrogenation of α-methylstyrene	variation of rate enhancement with cycle period predicted

unsteady state operation, namely, liquid flow modulation, to demonstrate its capability. The effects of liquid flow modulation parameters, such as amplitude (liquid flow), cycle period, split (fraction of the cycle period with liquid flow), and extent of gas and liquid limitation, are simulated for a test reaction case.

Model Development

This section discusses the development of a generalized model, which can account for phenomena occurring in trickle bed reactors under unsteady state periodic operating conditions. The features common to previous models such as the bulk phase species and energy balance equations are presented briefly to begin with, followed by the features of this model used in modeling source terms for these equations which are presented in greater detail. The key assumptions in the model are primarily made to reduce the computational complexity as follows:

1. Variation of temperature, concentration, velocity, and holdup in the radial direction is negligible as compared to axial direction. Hence a one-dimensional (1-D) system is considered. However, bed nonuniformity in industrial scale trickle bed reactors can lead to lateral gradients which need to be accounted for in more detailed description than the current 1-D approach.

2. All the parameter values are equal to the cross sectionally averaged values and vary only with axial location and time. These are determined at every time instant for all the axial locations and are used to solve for pertinent variables at the next instant in time.

3. The heat of reaction is released only to the solid (catalyst) and then transferred to other phases through interphase heat transfer.

4. The catalyst pellets are assumed to be fully internally wetted. Hence, no temperature gradients are assumed to exist inside them. However, for partial internal wetting, the approach of Harold et al.[24] and Khadilkar et al.[25] needs to be followed.

5. The catalyst pellets are modeled as slabs of three types based on external wetting conditions: fully externally wetted, half-wetted, and fully dry (different approaches to solution of catalyst level equations are discussed later).

Model Equations

Bulk Species Transport. The dynamic variation in the liquid and gas phase species concentrations is obtained by solving the unsteady state species mass balance equations, consisting of accumulation, convection, and interphase transport for the gas and liquid phases written as eqs 1 and 2, respectively.

$$\frac{\partial}{\partial t}(\epsilon_L C_{iL}) + \frac{\partial}{\partial z}(u_{IL}\epsilon_L C_{iL}) = N_i^{GL} a_{GL} - N_i^{LS} a_{LS} \quad [nc-1] \quad (1)$$

$$\frac{\partial}{\partial t}(\epsilon_G C_{iG}) + \frac{\partial}{\partial z}(u_{IG}\epsilon_G C_{iG}) = -N_i^{GL} a_{GL} - N_i^{GS} a_{GS} \quad [nc-1] \quad (2)$$

Note that numbers in brackets indicate the number of such equations available. Only nc − 1 equations are written above and the continuity equation is written for

each phase to complete the equation set (nc is the number of components).

Bulk Energy Transport. A three-temperature model with catalyst, liquid, and gas possibly having different temperatures is considered to be consistent with the solution of interphase energy balance equations (discussed later).

The gas phase energy balance can be written in terms of the accumulation, convection terms, and a loss term to the ambient atmosphere (which is omitted in the adiabatic calculations).

$$\frac{\partial(\rho_G \epsilon_G H_G)}{\partial t} + \frac{\partial(\rho_G \epsilon_G u_{IG} H_G)}{\partial z} = -E^{GL} a_{GL} - E^{GS} a_{GS} - E^{GA} a_{GA} \qquad [1] \quad (3)$$

Similarly, considering the energy balance for the liquid phase in terms of accumulation and convection terms and gas to liquid heat transfer, solid to liquid heat transfer, and heat loss to ambient, we have

$$\frac{\partial(\rho_L \epsilon_L H_L)}{\partial t} + \frac{\partial(\epsilon_L u_{IL} \rho_L H_L)}{\partial z} = E^{GL} a_{GL} - E^{SL} a_{SL} - E^{LA} a_{LA} \qquad [1] \quad (4)$$

The immobile catalyst is assumed to be fully internally wetted and to have no internal temperature gradients. The temporal temperature variation also contains the axial dependence due to the interface energy flux terms on the right-hand side of the energy equation and is obtained by solution of the energy balance for the solid catalyst:

$$\frac{\partial(1-\epsilon_B) H_{CP}}{\partial t} = E^{LS} a_{LS} + E^{GS} a_{GS} \qquad [1] \quad (5)$$

Continuity Equation for the Flowing Liquid and Gas. The variation of liquid holdup with time and axial position is obtained by solving the continuity equations for the liquid and the gas phase. The liquid holdup inside the catalyst particles is considered to be constant as it is assumed fully wetted catalyst particles. However, the liquid present in the reactor is divided into flowing liquid and stagnant (intracatalyst) liquid to improve tractability in modeling. The continuity equation for the flowing liquid and gas is written in terms of the accumulation and convection terms balanced by the total mass transferred to and from the other phases (written in terms of interphase fluxes for gas−liquid, liquid−solid, and gas−solid equations, each discussed in the next section).

$$\frac{\partial \rho_L \epsilon_L}{\partial t} + \frac{\partial(\rho_L u_{IL} \epsilon_L)}{\partial z} = +\sum N_i^{GL} a_{GL} M_i - \sum N_i^{LS} a_{LS} M_i \qquad [1] \quad (6)$$

$$\frac{\partial \rho_G \epsilon_G}{\partial t} + \frac{\partial(\rho_G u_{IG} \epsilon_G)}{\partial z} = -\sum N_i^{GL} a_{GL} M_i - \sum N_i^{GS} a_{GS} M_i \qquad [1] \quad (7)$$

The variation of interstitial phase velocity with time and axial position is calculated by solving the liquid and gas phase momentum balance equations. The momentum equations for the flowing liquid and gas phase can be written in terms of accumulation and convection terms on the left-hand side, and the gravity, pressure gradient, drag due to the packed phase, gas−liquid interphase momentum exchange (with exchange coefficient K), and momentum gain due to interphase mass exchange terms on the right-hand side, as

$$\frac{\partial}{\partial t}(\rho_L u_{IL} \epsilon_L) + \frac{\partial}{\partial z}(\rho_L \epsilon_L u_{IL} u_{IL}) = \epsilon_L \rho_L g - \epsilon_L \left.\frac{\partial P}{\partial z}\right|_L - F_{D,Liq} + K(u_{IG} - u_{IL}) + u_{IL}^I [\sum N_i^{GL} a_{GL} M_i - \sum N_i^{LS} a_{LS} M_i] \qquad [1] \quad (8)$$

$$\frac{\partial}{\partial t}(\rho_G u_{IG} \epsilon_G) + \frac{\partial}{\partial z}(\rho_G \epsilon_G u_{IG} u_{IG}) = \epsilon_G \rho_G g - \epsilon_G \left.\frac{\partial P}{\partial z}\right|_G - F_{D,Gas} + K(u_{IL} - u_{IG}) + u_{IG}^I [-\sum N_i^{GL} a_{GL} M_i - \sum N_i^{GS} a_{GS} M_i] \qquad [1] \quad (9)$$

It is assumed here that the mass exchange occurs at the interfacial velocities for liquid and gas phases, u_{IL}^I and u_{IG}^I, respectively. The momentum exchange coefficient (K) between the gas and the liquid is obtained from a gas−liquid drag coefficient[26] or dropped for the case of low interaction between gas and liquid in trickle flow at very low liquid velocities. The drag term (F_D) is due to the solid phase and is obtained from well accepted extensions of the Ergun equation to two phase flow as below.[27]

$$F_{D,Gas} = \epsilon_G \rho_G g \left(\frac{\epsilon}{\epsilon - \epsilon_L}\right)^3 \left[\frac{E_1 \, Re_{G,F}}{Ga_G} + \frac{E_2 \, Re_{G,F}^2}{Ga_G}\right] \qquad [1] \quad (10)$$

$$F_{D,Liq} = \epsilon_L \rho_L g \left(\frac{\epsilon}{\epsilon_L}\right)^3 \left[\frac{E_1 \, Re_{L,F}}{Ga_L} + \frac{E_2 \, Re_{L,F}^2}{Ga_L}\right] \qquad [1] \quad (11)$$

Gas−liquid, liquid−solid, and gas−solid mass transfer is modeled by the Stefan−Maxwell equations for multicomponent transfer as discussed in the following sections.

Interphase Mass and Energy Transport by the Stefan−Maxwell Formulation. All the interphase fluxes (gas−liquid, liquid−solid, and gas−solid) need to be modeled for unsteady state periodic operation due to the fact that assumptions for conventional isothermal, steady state dilute solution transport of single species are not justified in the unsteady state periodic operation case. Since flow rates can change with time and axial position by a large magnitude, any assumption of simple (or equilibrium) mass or heat transfer being the controlling mechanism does not hold true for the entire cycle period. Hence, the use of Stefan−Maxwell equations is required to accurately model the interphase fluxes at each time instant in these situations.[28,29] The solution of the Stefan−Maxwell problem involves the formulation of the transport and equilibrium relations at each interface, which are then solved for the required fluxes and compositions. For example, in case of the gas−liquid interface, the unknown variables (for a system with nc number of components) are the nc interphase fluxes, the nc interface mole fractions at liquid and vapor interface each, and the interface temperature which add up to a

Table 3. Typical Vector of the Stefan–Maxwell Equations at the Gas–Liquid Interface

$$F_{GL}(z,t)=\begin{bmatrix}
N_1^{GL}-c_{tl}\sum_j\{[\beta_L][k_L^o][\Gamma]\}_{1,j}(x_j^I-x_j^L)-x_1(\Delta q)/\lambda_x\\
N_2^{GL}-c_{tl}\sum_j\{[\beta_L][k_L^o][\Gamma]\}_{2,j}(x_j^I-x_j^L)-x_2(\Delta q)/\lambda_x\\
\vdots\\
N_{nc-1}^{GL}-c_{tl}\sum_j\{[\beta_L][k_L^o][\Gamma]\}_{nc-1,j}(x_j^I-x_j^L)-x_{nc-1}(\Delta q)/\lambda_x\\
N_1^{GL}-c_{tg}\sum_j\{[\beta_G][k_G^o]\}_{1,j}(y_j^V-y_j^I)-y_1(\Delta q)/\lambda_y\\
N_2^{GL}-c_{tg}\sum_j\{[\beta_G][k_G^o]\}_{2,j}(y_j^V-y_j^I)-y_2(\Delta q)/\lambda_y\\
\vdots\\
N_{nc-1}^{GL}-c_{tg}\sum_j\{[\beta_G][k_G^o]\}_{nc-1,j}(y_j^V-y_j^I)-y_{nc-1}(\Delta q)/\lambda_y\\
y_1^I-K_1x_1^I\\
y_2^I-K_2x_{21}^I\\
\vdots\\
y_{nc}^I-K_{nc}x_{nc}^I\\
x_1^I+x_2^I+x_3^I+\ldots x_{nc}^I-1\\
y_1^I+y_2^I+y_3^I+\ldots y_{nc}^I-1\\
q_V-q_L+\sum_{i=1}^{n}N_i^{GL}(H_i^V-H_i^L)
\end{bmatrix}_{3nc+1,1}$$

Liquid Side Flux Equations

Gas Side Flux Equations

Interface Equilibrium Equations

Mole Fraction Summation

Energy Balance 'Bootstrap'

total of 3(nc) + 1 unknowns. The equations available for solution are the liquid and gas phase absolute flux equations (nc − 1 independent equations each), the equilibrium relations at the interface (nc), the mole fraction summation constraints for the gas and liquid interface (2). It is important to note that only nc − 1 independent equations can be written for the absolute fluxes, which are based on relative fluxes and hence are subject to the Gibbs–Duhem restriction (see Appendix A for more details). The extra condition needed to complete the set of equations, often referred to as the "bootstrap"[28] depends upon additional information about the physics of the problem. Several alternatives such as Stefan diffusion, Graham diffusion, equimolar counterdiffusion, etc. have been used as bootstraps due to their applicability to specific physical situations. However, in unsteady state operation, the only condition that is consistently applicable is the energy balance relation itself. This condition is usually written in the form of a matrix [β] which incorporated in the matrix form of the multicomponent transport coefficient [k] (as defined in Appendix A) to form the gas–liquid interphase flux equation.

$$N_i^{GL}-c_{tl}\{[\beta_L][k_L^o][\Gamma]\}_{i,j}(x_j^I-x_j^L)-x_i(\Delta q)/\lambda_x=0 \qquad [nc-1] \quad (12)$$

The contribution of the term containing Δq is due to the net conductive heat flux at the interface and is evaluated as given in Appendix A. The thermodynamic nonideality is accounted for as needed by incorporation of the matrix [Γ] of activity coefficients as defined in Appendix A. Similar equations can be written for the gas side as given in Appendix A. It is assumed here that the interface reaches equilibrium instantaneously, and that there is no accumulation of the species at the interface which allows the use of eq 13. The equilibrium

$$y_i^I=K_i^I(x_I, y_I, T_I)x_i^I \qquad [nc] \qquad (13a)$$

constants are determined using a suitable activity coefficient model, such as Wilson's, which is employed for the test case in this study (as given in Appendix A). The transport coefficients [k] are corrected for high flux based on the algorithm suggested by Taylor and Krishna[28] (as shown in Appendix A). Similar equations can be written for the gas side transport as done for the liquid resulting in the complete set of equations expressed in Table 3 as a vector of the functions to be solved for. To account for gas phase nonideality in some reactions such as hydrosulfurization (HDS) at high pressure and temperature, the fugacity correction factors should be considered as follows:

$$y_i^I=\left\{\frac{\gamma_i p_i^{sat}}{\phi_k P}\right\}^I x_i=K_i^I x_i^I \qquad (13b)$$

Combined Solution of Stefan–Maxwell Equations at the Liquid–Solid and Gas–Solid Interface. The catalyst pellets are assumed to be half-wetted slabs with flowing liquid and gas on either side (as shown in Figure 1 and discussed in detail in the next section). The unknowns at the liquid–solid interface of the catalyst are the nc liquid–solid fluxes, nc liquid–solid interface compositions, and one liquid–solid interface temperature (total 2(nc) + 1). The liquid–solid transport equations can be formulated via the Stefan–

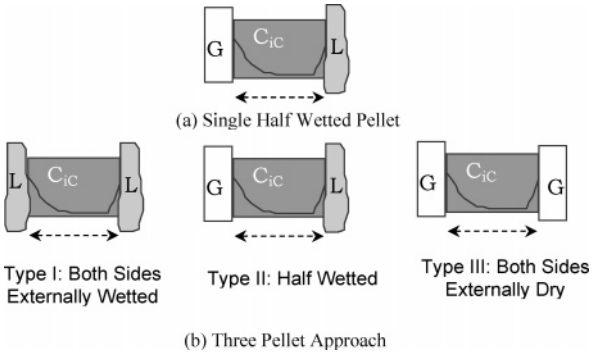

Figure 1. Schematic representation of the externally partially wetted catalyst.

Table 4. Typical Vector of the Stefan–Maxwell Equations for a Half Wetted Pellet

$$
F_{GLS}(z,t)=\begin{bmatrix}
N_1^{LS}-c_{tl}\sum_j\{[\beta_L][k_L^\circ][\Gamma]\}_{1,j}(x_j^L-x_j^I)-x_1(\Delta q)/\lambda_x\\
N_2^{LS}-c_{tl}\sum_j\{[\beta_L][k_L^\circ][\Gamma]\}_{2,j}(x_j^L-x_j^I)-x_2(\Delta q)/\lambda_x\\
\vdots\\
N_{nc-1}^{LS}-c_{tl}\sum_j\{[\beta_L][k_L^\circ][\Gamma]\}_{nc-1,j}(x_j^L-x_j^I)-x_{nc-1}(\Delta q)/\lambda_x\\
N_1^{CP}-c_{tCP}\sum_j\{[\beta][B]^{-1}[\Gamma]\}_{1,j}(\nabla x|_{LSI})\\
N_2^{CP}-c_{tCP}\sum_j\{[\beta][B]^{-1}[\Gamma]\}_{2,j}(\nabla x|_{LSI})\\
\vdots\\
N_{nc-1}^{CP}-c_{tCP}\sum_j\{[\beta][[B]^{-1}[\Gamma]\}_{nc-1,j}(\nabla x|_{LSI})\\
N_1^{GS}-c_{tG}\sum_j\{[\beta_G][k_G^\circ]\}_{1,j}(y_j^G-y_j^I)-y_1(\Delta q)/\lambda_y\\
N_2^{GS}-c_{tG}\sum_j\{[\beta_G][k_G^\circ]\}_{2,j}(y_j^G-y_j^I)-y_2(\Delta q)/\lambda_y\\
N_{nc-1}^{GS}-c_{tG}\sum_j\{[\beta_G][k_G^\circ]\}_{nc-1,j}(y_j^G-y_j^I)-y_{nc-1}(\Delta q)/\lambda_y\\
N_1^{CP}-c_{tCP}\sum_j\{[\beta][B]^{-1}[\Gamma]\}_{1,j}(\nabla x|_{GSI})\\
N_2^{CP}-c_{tCP}\sum_j\{[\beta][B]^{-1}[\Gamma]\}_{2,j}(\nabla x|_{GSI})\\
N_{n-1}^{CP}-c_{tCP}\sum_j\{[\beta][[B]^{-1}[\Gamma]\}_{n-1,j}(\nabla x|_{GSI})\\
(y_1^I-K_1x_1^I)_{GS}\\
(y_2^I-K_2x_{21}^I)_{GS}\\
\vdots\\
(y_{nc}^I-K_{nc}x_{nc}^I)_{GS}\\
(x_1^I+x_2^I+x_3^I+\ldots x_{nc}^I)_{GS}-1\\
(x_1^I+x_2^I+x_3^I+\ldots x_{nc}^I)_{LS}-1\\
(y_1^I+y_2^I+y_3^I+\ldots y_{nc}^I)_{GS}-1\\
q_G-q_S+\sum_{i=1}^{nc}N_i(H_i^G-H_i^S)\\
q_L-q_S+\sum_{i=1}^{nc}N_i(H_i^L-H_i^S)\\
(\sum N_iM_i/\rho_{Li})_{LSI}=(\sum N_iM_i/\rho_{Li})_{GSI}
\end{bmatrix}_{5nc+2,1}
$$

Liquid Solid Interface Flux Equations

Catalyst Boundary Condition Flux Equations

Gas Solid Interface Flux Equations

Catalyst Boundary Condition Flux Equations

Gas Solid Interface Equilibrium Equations

Mole Fraction Summations

Energy Balance Equations

'Bootstrap' Equation

Maxwell scheme by writing the flux equations in the general form

$$(N^{LS}) = c_t[\beta_{LS}][k^{\bullet}_{LS}](\Delta x) \quad [nc-1] \qquad (14)$$

The independent equations that can be written for the liquid–solid interface are the nc − 1 mass transfer flux equations on the liquid side, and the nc − 1 equations for the intracatalyst wetted side fluxes from the reaction–diffusion equations, one equation from the interface mole fraction summation constraint, and one for the energy flux equation (as listed in Table 4). The additional "bootstrap" equation required for complete definition of the problem is chosen to ensure constant liquid volume in the pellet by applying a zero net volumetric flux condition. It must be noted here that we have assumed a completely internally wetted pellet to be consistent with observations in the literature.[6,8] The bootstrap matrix calculation on the liquid side is still based on the energy balance equation, whereas on the catalyst side, the above-mentioned zero volumetric flux condition is implemented as

$$(\sum N_iM_i/\rho_{Li})_{L-S} = (\sum N_iM_i/\rho_{Li})_{G-S} \qquad [1] \qquad (15)$$

The equations for the externally dry side of the catalyst are similar to the gas–liquid interface equations discussed earlier. The number of unknowns in this case is 3(nc) + 1 as listed in Table 4. The two sets of equations are coupled through the catalyst level reaction–diffusion equations as they incorporate the boundary conditions for the pellet scale model equations. The bootstrap condition used here is the same as that used on the liquid–solid interface in order to keep the entire set of equations consistent. This condition also acts as the coupling between the gas–solid and the liquid–solid sides of the catalyst. This completes the set of equations that is necessary to solve for all the transport processes on the liquid–solid and gas–solid interfaces (5(nc) + 2 total equations). It remains to list the catalyst level equations, which are discussed next.

Solid Phase Species Balance Equations. Catalyst level equations of the unsteady reaction–diffusion type need to be solved at each axial location to obtain the intracatalyst species concentration and reaction rate. To introduce the effect of dynamic wetting and supply of reactants, a slab model[24,25,31–33] with either side exposed to gas and liquid is postulated as shown in Figure 1. This simplification has been made in the literature to simulate the effects of partial wetting

Table 5. Energy Flux Equations for Gas−Liquid, Liquid−Solid, and Gas−Solid Interfaces

Gas−Liquid Interface

$E^{G} = h_G^{\bullet}(T_G - T_{GL}^{I}) + \sum_{i=1}^{n} N_i^{GL}\,\overline{H_i^{G}}(T_G)$

$E^{L} = h_L^{\bullet}(T_{GL}^{I} - T_L) + \sum_{i=1}^{n} N_i^{GL}\,\overline{H_i^{L}}(T_L)$

interface equilibrium: $E^{L} = E^{G} = E^{GL}$

Liquid−Solid Interface

$E^{S} = h_S^{\bullet}(T_{LS}^{I} - T_S) + \sum_{i=1}^{n} N_i^{LS}\,\overline{H_i^{S}}(T_S)$

$E^{L} = h_L^{\bullet}(T_L - T_{LS}^{I}) + \sum_{i=1}^{n} N_i^{LS}\,\overline{H_i^{L}}(T_L)$

interface equilibrium: $E^{L} = E^{S} = E^{LS}$

Gas−Solid Interface

$E^{G} = h_G^{\bullet}(T_G - T_{GS}^{I}) + \sum_{i=1}^{n} N_i^{GS}\,\overline{H_i^{G}}(T_G)$

$E^{S} = h_S^{\bullet}(T_{GS}^{I} - T_S) + \sum_{i=1}^{n} N_i^{GS}\,\overline{H_i^{S}}(T_S)$

interface equilibrium: $E^{G} = E^{S} = E^{GS}$

overall gas phase enthalpy per unit mass (H_G):
$H_G = \sum C_{iG}\bar{H}_{iG}/\rho_G$,
$\bar{H}_{iG}$ = molar enthalpy of each species in the gas phase
overall liquid phase enthalpy per unit mass (H_L):
$H_L = \sum C_{iL}\bar{H}_{iL}/\rho_L$,
$\bar{H}_{iL}$ = molar enthalpy of each species in the liquid phase
overall enthalpy of the catalyst per unit volume (H_{CP}):
$H_{CP} = (1 - \epsilon_P)C_{CP}(T_{CP} - T_{ref}) + \epsilon_P \sum C_{iCP}\bar{H}_{iCP}$,
$\bar{H}_{iCP}$ = molar enthalpy of each species in the catalyst pellet

(which in reality may vary between 0% and 100%). The general equation can be given as

$$\frac{\partial C_{i\mathrm{CP}}}{\partial t} + \frac{\partial N_{i\mathrm{CP}}}{\partial(\mathrm{zc})} = \nu_i R \qquad [\mathrm{nc}] \tag{16}$$

This relation has to be solved in conjunction with the boundary conditions of flux from the wetted and dry face which are directly obtained from the solution of the reactor scale liquid and gas species concentration profiles from solution of equations in Tables 3 and 4. Although there is no explicit appearance of the reactor dimension in the above equation, it is implicit in the boundary conditions imposed at every point in the reactor and hence has to be solved separately at each point in the reactor.

Three approaches are considered as alternatives to solve the catalyst level equations and are discussed (with pros and cons of each approach) below. The intracatalyst mass transfer is calculated on the basis of the effective diffusivity (De) calculated from standard correlations.[4]

(i) Single Half-Wetted Pellet Approach. Here we consider a single internally fully wetted but externally half-wetted pellet exposed to the flowing liquid on one side and flowing gas on the other (Figure 1a). For the intracatalyst calculations, the flux of species i, $N_{i\mathrm{CP}}$ (in eq 16), can be expressed in terms of the Stefan−Maxwell diffusion matrix as a product of the inverse of the diffusion matrix and the nonideality matrix $[B]^{-1}[\Gamma]$ as done for the gas−liquid and gas−liquid−solid transport. However, since both these matrices are functions of compositions and fluxes, it significantly complicates the solution of the reaction−diffusion equations, which now have to be solved in three dimensions i.e., catalyst length, time, and concentration in addition to the reactor dimension. The equations for this formulation (written for nc − 1 species) in terms of a central finite difference scheme for the spatial derivatives are as shown in Table 6. Although this approach has been demonstrated for steady state operation,[24,25] it has the following disadvantages for unsteady state operation. First, it assumes a half-wetted pellet at all times and axial locations, which is not the case in the system of interest, since flow modulation may cause the change in pellet condition from fully externally wetted to half-wetted, and fully externally dry. Second, this approach assumes constant wetting conditions at all temporal and spatial locations, which makes it suitable only for steady state simulation. Finally, the total number of equations ((nc −1) × (ncat − 1)) is prohibitively large to be solved at each axial location and at each time instant due to the use of finite differences (where the discretization points, ncat, required to capture the concentration profiles of all species can be quite large).

(ii) Three Pellet Apparent Rate Form. This approach accounts for the three possible external wetting conditions for a completely internally wetted slab type catalyst, i.e., it considers three types of pellets which can have (i) both sides wetted, (ii) a half-wetted pellet, and (iii) a pellet with both sides externally dry (Figure 1b). The actual distribution of the wetted and dry sides of the three pellets is assigned on the basis of catalyst wetting efficiency calculated from well-known empirical correlations[34,35] at each time instant at the local flow conditions. For example, at a locally calculated wetting efficiency of 50%, we would assign a pellet with both sides wetted, a pellet with a dry and a wetted side, and one with both sides dry in order to achieve the necessary resolution with minimum number of pellets (three). Implementation of this formulation for the present case necessitates the use of three times the number of equations than when a single pellet is used and a correspondingly large computational effort. However, for the present case, this is simplified by using the apparent rates with locally calculated effectiveness factors, and we assume that the reaction occurs either at the apparent rate at the interface or at the intrinsic rate in the bulk of the catalyst. This assumption is realistic only at the two extremes, i.e., very high Thiele modulus (reaction near the surface) and very low Thiele modulus (reaction inside the catalyst), but is not suitable for intermediate values of Thiele moduli. Nevertheless, it is used here due to its advantage of allowing all the multiple wetting conditions discussed above and due to its ability to simulate the accumulation of the nonlimiting reactant in the catalyst, which can then be consumed during another part of the transient cycle. The governing equations for this case for a half-wetted pellet (with sides a and b) are

$$c_{\mathrm{tCP}}\frac{x_i^{\mathrm{nt}+1} - x_i^{\mathrm{nt}}}{\mathrm{d}t} - \sum_{j=1\mathrm{a},1\mathrm{b}} N_i^{\mathrm{LS}} a_j^{\mathrm{LS}} - \sum_{j=1\mathrm{a},1\mathrm{b}} N_i^{\mathrm{GS}}\, a_j^{\mathrm{GS}} - \nu_1 R_{\mathrm{App}}^{\mathrm{nt}+1} - \nu_1 R_{\mathrm{bulk}}^{\mathrm{nt}+1} = 0 \qquad [\mathrm{nc}] \tag{17}$$

(iii) Three Pellet Form. The disadvantages of both approaches discussed above, i.e., the inability to model multiple wetting conditions (approach i) and the apparent rate approximation (approach ii), can in part be overcome by using a collocation solution[36] for the spatial derivative in a three-pellet rigorous model. This requires fewer computational points and hence a lesser number of equations to be solved than the finite difference version of approach i. Also, it does not have the shortcomings of approach ii, but does require an enormous amount of extra computational effort in solution of the catalyst level equations, particularly since both the multicomponent formulation and the collocation solution involve matrices (for diffusivity ($[\beta][B]^{-1}[\Gamma]$) and

Table 6. Reaction−Diffusion Equation Set for a Single Pellet Model

$$F_{CAT}(z,t)=\begin{bmatrix} c_{tCP}\dfrac{x_{1,zc}^{nt+1}-x_{1,zc}^{nt}}{dt}-c_{tCP}\sum_j\{[\beta][B]^{-1}[\Gamma]\}_{1,j}\dfrac{(x_{j,zc+1}^{nt+1}-2x_{j,zc}^{nt+1}+x_{j,zc-1}^{nt+1})}{(\Delta zc)^2}-\nu_1 R_{zc}^{nt+1} \\ c_{tCP}\dfrac{x_{2,zc}^{nt+1}-x_{2,zc}^{nt}}{dt}-c_{tCP}\sum_j\{[\beta][B]^{-1}[\Gamma]\}_{2,j}\dfrac{(x_{j,zc+1}^{nt+1}-2x_{j,zc}^{nt+1}+x_{j,zc-1}^{nt+1})}{(\Delta zc)^2}-\nu_2 R_{zc}^{nt+1} \\ \vdots \\ c_{tCP}\dfrac{x_{nc-1,zc}^{nt+1}-x_{nc-1,zc}^{nt}}{dt}-c_{tCP}\sum_j\{[\beta][B]^{-1}[\Gamma]\}_{nc-1,j}\dfrac{(x_{j,zc+1}^{nt+1}-2x_{j,zc}^{nt+1}+x_{j,zc-1}^{nt+1})}{(\Delta zc)^2}-\nu_{nc-1} R_{zc}^{nt+1} \end{bmatrix}_{nc-1,ncat-1}$$

Table 7. Catalyst Level Reaction−Diffusion Equations for the Three Pellet Model[a]

$$F_{CAT}(z,t)=\begin{bmatrix} \dfrac{c_{1,ic}^{nt+1}-c_{1,ic}^{nt}}{dt}-\sum_{isp=1}^{nc-1}\sum_{jj=1}^{ncol}\{[\beta][B]^{-1}[\Gamma]\}_{1,isp}[B_{col}]_{ic,jj}\bar{c}_{isp,jj}-\nu_1 R_{ic}^{nt+1} \\ \vdots \\ (ic=1,2,....ncol \text{ for species 1, pellet I}) \\ \dfrac{c_{2,ic}^{nt+1}-c_{2,ic}^{nt}}{dt}-\sum_{isp=1}^{nc-1}\sum_{jj=1}^{ncol}\{[\beta][B]^{-1}[\Gamma]\}_{2,isp}[B_{col}]_{ic,jj}\bar{c}_{isp,jj}-\nu_2 R_{ic}^{nt+1} \\ \vdots \\ (ic=1,2,....ncol \text{ for species 2, pellet I}) \\ \dfrac{c_{nc-1,ic}^{nt+1}-c_{nc-1,ic}^{nt}}{dt}-\sum_{isp=1}^{nc-1}\sum_{jj=1}^{ncol}\{[\beta][B]^{-1}[\Gamma]\}_{2,isp}[B_{col}]_{ic,jj}\bar{c}_{isp,jj}-\nu_{nc-1} R_{ic}^{nt+1} \\ \vdots \\ (ic=1,2,....ncol \text{ for species 3, pellet I}). \\ \vdots \\ ncol*(nc-1) \text{ equations for each pellet} \end{bmatrix}_{3(nc-1)ncol}$$

[a] ic and isp are species indices, ncol is the number of collocation points, and nt is the time level.

spatial second derivatives [B_{col}], respectively). The set of equations are much more complex in this case as formulated in Table 7, but the expressions are more rigorous than given in the three pellet apparent rate approach. Although the code for this approach was developed, the results presented and discussed here are based only on approach ii due to computational limitations of approach iii.

Solution Strategy for Reactor and Pellet Scale Equations. Several approaches that have been suggested in the literature for numerical solution of hyperbolic partial differential equations were considered as alternatives. The traditional and elegant moving boundary approach[37] was found to be unsuitable for the present problem due to the different phases moving at different velocities (i.e., a stationary solid phase, a pulsing liquid phase, and a constant velocity gas phase). Another popular approach considered was the use of orthogonal collocation on finite elements (OCFEM),[36,38] which is known to work very well for nonsteep concentration and temperature profiles. Unfortunately this was not the case in the present problem. The use of multicomponent transport equations added a large set of simultaneous nonlinear algebraic equations for the interphase fluxes, temperatures, and concentrations and prevented the use of an ordinary differential equation (ODE) solver (such as LSODE[39] and DDASSL with method of lines,[40] PDECOL[41]). Matrix solution of the interphase transport could not be handled by other packages such as gPROMS[42] which can solve integral, partial differential, and algebraic equations (IPDAE solver). The approach that was finally successful in solving the present set of equations was to solve the bulk species and energy equations by marching in space using a semiimplicit predictor−corrector approach. The values obtained from the predictor step for all concentrations and temperatures were used as guessed values for a fully implicit corrector step that simultaneously solves for mass and energy flux source terms to the above-mentioned set of equations. These source terms involve evaluation of interphase mass and energy fluxes, interface concentrations, and temperatures by solution of nonlinear equations at the interface via a globally convergent multivariable Newton solver with a line search algorithm incorporated into it.[43] This algorithm uses the direction of the variable correction toward the desired root obtained from Newton's method and finds the optimal step to be taken at each iteration by a line search algorithm over the specified search domain. It also allows a check for local and global solution by a function minimization algorithm, which is part of the set of solver routines.

For the purpose of spatial discretization, all the concentrations, temperatures, and other scalar variables are defined at the cell centers of a staggered grid which is employed here for convenience in solution of pressure and velocities in the flow solver discussed in the next subsection. It is convenient in many cases to nondimensionalize the equations using the characteristic values of each variable to obtain the familiar dimensionless groups. Dimensionless quantities were not used here due to unavailability of characteristic parameters, which would be valid for the spatial and temporal variation. However, for improved convergence of the Newton routines, local nondimensionalization was employed based on variables at previous time and spatial location. The Newton solver required a user supplied analytical Jacobian for computational efficiency. However, in this case, the analytical Jacobian evaluation proved insufficient due to the absence of explicit terms containing the (nc)th variable (in the flux equations in Tables 3 and 4 and eq 17). Hence a numerical Jacobian evaluated by a finite difference approximation was used.

The fluid dynamic such as phase holdups and velocities is solved at each time step for the entire reactor before the rest of the solution is attempted for the next time instant. The flow simulation involves a semiimplicit solution for the velocity and hence limits the time step taken in the reaction-transport solver. This is partly compensated by the use of multiple substeps in the flow solver as discussed in the flow solution strategy presented next.

Solution of Continuity and Momentum Balance Equations. The approach used to solve the continuity and momentum equations is based on the semiimplicit MAC (marker and cell) method.[44−46] It is implicit in pressure and exchange terms, and, explicit in all other terms such as gravity, drag, and convection. A staggered

grid is used for scalars, pressure, and phase holdups, which are evaluated at the midpoint of the computational cell, whereas vectors such as velocity, drag, etc. are evaluated at the cell faces themselves following the approach used in typical computational fluid dynamic (CFD) formulations.[46,47] An assumption made here is that both the phases are incompressible.

The solution algorithm consists of three main steps. The calculations at each of these steps are as described below, and detailed equations are presented in Appendix B.

Step 1: The momentum equation is evaluated explicitly (at the nth time instant) using velocity, holdup, and pressure at that instant to obtain an estimate of the velocities at the next ((n + 1)th) time instant. The velocities obtained at this step do not satisfy continuity and are considered as intermediate calculation variables.

Step 2. The intermediate velocities are used to evaluate the pressure correction for the next time instant by solution of the Poisson equation for pressure.

Step 3. The evaluation of the phase velocities and holdups at the new time instant is based on the newly evaluated pressure, which ensures that continuity is satisfied. Repeating the calculation with time step halving ensures the accuracy and stability of the solution.

Results and Discussion

Although the development of the model presented above is generic in nature, some of the assumptions made are specific to the application of periodic liquid flow modulation for which the model is created, and the results of such simulations are presented here. Typical liquid flow modulation involves cycling of the liquid flow in the form of square waves with a given amplitude and frequency and with an average flow rate which corresponds to the flow rate value at steady state to which the reactor performance is compared. Liquid flow may be modulated between a high and a low value, with the low value being zero in many cases. Total cycle time is thus a sum of the high (referred to as PEAK or ON) flow and the low (referred to as BASE or OFF) flow time period of the cycle, and the high (PEAK or ON) fraction is referred to as the cycle split. The results presented here were obtained for the case of the hydrogenation reaction of α-methylstyrene to cumene on a palladium catalyst. It is noteworthy that modeling this particular reaction systems does not need the complexity of the multicomponent transport presented in the model. However, this reaction system is used because it has been studied extensively at steady state under gas reactant limited (low pressure, high liquid reactant concentration) and liquid reactant limited (high pressure, low liquid reactant concentration) conditions.[33] However, since most of the reported experimental data pertain to the gas reactant limited conditions, the unsteady state simulations presented here are restricted to those sets of conditions reported in Khadilkar et al.[48] Furthermore, simulation of performance enhancement under liquid limited conditions requires a detailed representation of the wetting and flow distribution phenomena in multiple reactor dimensions which is not in the scope of the present one-dimensional representation. The results presented and discussed next are sequenced so as to demonstrate the capability of flow simulation, reactor and catalyst scale species concentration simulation, and finally full cycle simulation to produce results for comparison with steady state operation as a function of typical flow modulation parameters. Experimental data corroborating the simulated results qualitatively are available in Khadilkar[11] and Khadilkar et al.[48] and the published literature (Table 1) and hence are not reproduced here graphically for sake of brevity. However, the key qualitative trends that illustrate the effect of flow modulation parameters are discussed.

Flow Simulation under Transient Conditions. In order to demonstrate the solution of momentum and continuity equations, a "cold flow" liquid velocity and holdup simulation during flow modulation is first considered. The periodically varying flow was simulated (reactor dimensions etc. given in Table 8) for a total cycle time of 80 s and liquid ON time of 15 s. Liquid velocity and liquid holdup for the duration of the total cycle are shown in Figures 2 and 3. The liquid flow rate used is 42 mL/min (mass velocity of 1.4 kg/(m^2 s)) during liquid ON time and 2 mL/min (mass velocity of 0.067 kg/(m^2 s)) during the rest of the cycle with a constant gas flow rate of 400 cm^3/min (0.0192 kg/(m^2 s)). These test results illustrate a typical flow modulation cycle. In reaction transport simulations, the code is executed first to reach steady state at the mean liquid flow rate and then the flow modulation is initiated. This changes the profiles shown in Figures 2 and 3 by making them start at some intermediate values corresponding to the mean flow instead of the near zero values shown. The reactor inlet velocity and holdup profile (corresponding to the liquid feed pulse) is seen to be sharp with significant spreading as the liquid pulse travels down the reactor. Upwind finite differences in space are used to capture the steep profiles at the feed without wiggles, which leads to some dissipation of the profile at the trailing edge of the pulse due to the elliptical nature of the pressure equation (see Appendix B). Dissipation error due to upwinding is typically proportional to $(\mu/\rho)\mathrm{Re}_{\Delta z}/2$ ($=U_{i\mathrm{L}}(\Delta z)/2$)[45] and is orders of magnitude smaller than the actual variables as long as at least 100 spatial discretization points are used. This dissipation is comparable to physical spreading (referred to as pseudoturbulent or viscous dissipation) of the flow in a trickle bed which is of the order of $U_{i\mathrm{L}}d_{\mathrm{p}}$.[52] Thus, the numerical dissipation inadvertently obtained from the numerical scheme is of the same order of magnitude and can be accepted as representing the physical dissipation so long as $\Delta z \leq 2d_{\mathrm{p}}$.

Reaction-Transport Simulation of Flow Modulation. The model equations proposed for solution of bulk species and energy transport along with the multicomponent interphase transport were tested for the α-methylstyrene hydrogenation reaction system. For this system, experimental results were available and indicate performance enhancement under gas reactant limited conditions (listed in Table 1). This reaction system consists of four components, reactants α-methylstyrene and hydrogen, product cumene, and solvent n-hexane. The reactor and catalyst specifications used in the simulation are given in Table 8. Even for a four component system, the number of equations to be solved at each time and axial location can be quite large. For example, for the three pellet apparent rate approach (approach ii discussed earlier), a set of 92 to 116 equations needs to be solved, depending upon the wetting conditions (fully externally wetted pellets, 92 equations; fully dry pellets, 116 equations). These equations originate from the implicit finite difference

Table 8. Reactor Dimensions, Operating Conditions and Parameter Estimation

Reactor Properties			
total length	59 cm	active catalyst length	26 cm
diameter	2.2 cm		
Operating Conditions			
superficial liquid mass velocity	0.05−2.5 kg/m^{2}s	operating pressure	30−200 psig (3−15 atm)
superficial gas mass velocity	3.3×10^{-3}−15×10^{-3} kg/m^{2}s	feed concentration	2.5−30% (200−2400 mol/m^3)
Catalyst Properties			
active metal	0.5% Pd	feed temp	20−25 °C
catalyst support	alumina	cycle time, τ (total period)	5−500 s
packing shape	sphere	cycle split, σ (ON flow fraction)	0.1−0.6
packing dimensions	3.1 mm	max. allowed temp rise	25 °C
bed porosity ϵ_B	0.4	catalyst area (S_X)	3×10^{-5} m^2
catalyst diameter	1.58×10^{-3} m	catalyst volume (V_P)	9.9×10^{-9} m^3
catalyst bulk density	1200 kg/m^3		
viscosity (liquid)	0.3×10^{-3} Pa.s	viscosity (gas)	0.008×10^{-3} Pa.s
density (liquid)	700 kg/m^3	density (gas)	1 kg/m^3

Parameter Estimation Correlations and References	
reaction rate form rate = kvs $(C_{AMS})^{\alpha} C_{H2}/(1 + K_1 C_{2AMS} + K_2 C_{Cumene})^{\beta}$ for low-pressure gas limited case $\alpha = \beta = K_1 = K_2 = 0$	Khadilkar[11]
thermal properties $(\Delta H_f)_G$, $(\Delta H_f)_L$, C_{pG}, C_{pL}	Reid et al.[49]
liquid phase infinite dilution diffusivity $D_{ij}^0 = (7.4 \times 10^{-12}) \dfrac{(\phi_j M_j)^{1/2} T}{\mu_j V_i^{0.6}}$	Wilke and Chang[50]
gas phase infinite dilution diffusivity $D_{ij}^0 = (1.013 \times 10^{-2}) \dfrac{((M_j + M_j)/M_i M_j)^{1/2} T^{1.75}}{P(V_i^{1/3} + V_i^{1/3})^2}$	Reid et al.[49]
correction of diffusivity for concentration using the Vignes correlation $D_{ij} = (D_{ij}^0)^{(1-x_i)} (D_{ji}^0)^{(x_i)}$	Krishna[29]
the film thickness (l) for gas and liquid phase (Sherwood correlation) $d_P/l = 0.023\ \mathrm{Re}^{0.83}\ \mathrm{Sc}^{0.44}$	Taylor and Krishna[28]
heat transfer coefficients for gas and liquid phase Nusselt number $h_\alpha d_P/k_\alpha = \mathrm{Pr}^{1/3}(2.14\ \mathrm{Re}^{1/2} + 0.99)$	Kern[51]
Chilton−Colburn analogy $h_\alpha = c_{t\alpha} C_{P\alpha} k_\alpha^{mt} (\mathrm{Pr/Sc})^{-2/3}$	Kern[51]
interfacial areas for interphase transport (gas−liquid, liquid−solid, and gas−solid) $a_{GL} = (3.9 \times 10^{-4})(1 - \epsilon_L/\epsilon_B)(1/d_P)\mathrm{Re}_L^{0.4}(d_P/D_R)^{-2}$ $a_{LS} = (1 - \epsilon_B)(V_P/S_X)\eta_{CE}$ $a_{GS} = (1 - \epsilon_B)(V_P/S_X)(1 - \eta_{CE})$	El-Hisnawi et al.[34]
catalyst wetting efficiency $\eta_{ce} = 1.617\ \mathrm{Re}_L^{0.146}\ \mathrm{Ga}_L^{-0.0711}$	El-Hisnawi et al.[34]
$\eta_{CE} = 1.104\ \mathrm{Re}_L^{0.33} \left[\dfrac{1 + [\Delta P/Z/\rho_L g]}{\mathrm{Ga}_L}\right]^{1/9}$	Al-Dahhan and Dudukovic[35]

approximation of the partial differential equations and the nonlinear algebraic equations resulting from the Stefan−Maxwell equations for the gas−liquid, liquid−solid, and gas−solid transport. These are then solved by the multivariable globally convergent Newton method discussed earlier.

Typical simulation runs of liquid flow modulation are carried out in two stages. The first stage involves simulation of the reaction to steady state at the mean flow rate to obtain the performance under steady state conditions. This is followed by simulation of one or more cycle periods with liquid flow ON and OFF (for ON−OFF flow modulation) or with liquid high and low flow (for BASE−PEAK flow modulation). During the first part of the simulation, the inlet velocity and holdup are specified along with the feed concentrations and temperatures. The velocity and holdup are then computed for the entire spatial domain at the next time instant as discussed earlier. The reaction transport equations are then solved at each axial location for that time instant. Figure 4 depicts the development of reactant (α-methylstyrene) concentration profiles at different axial locations with time for a gas limited reaction case ($C_{\alpha-MS,feed} = 1484$ mol/m^3 at an operating pressure of 1 atm). Figure 5 shows the corresponding development of product (cumene) profiles in the reactor. It should be noted that the α-methylstyrene concentration profiles reach pseudo steady state values relatively early as compared to the cumene concentration profiles shown in Figure 5. The hydrogen concentration in the liquid phase shows a very interesting behavior as presented in Figure 6. The hydrogen concentration builds to saturation at the reactor exit where no α-methylstyrene is present at the beginning of the cycle. At the reactor inlet, it is consumed faster than can be transferred from the gas phase and results in much lower concentration. As liquid reactant (α-methylstyrene) reaches each point in the reactor, the hydrogen concentration drops to its steady state values. Since this simulation is done at conditions of a gas limited reaction, the hydrogen

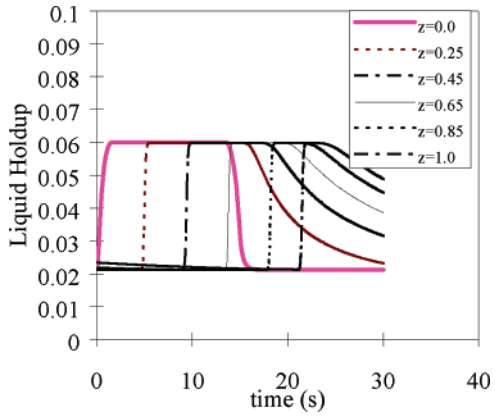

Figure 2. Transient liquid holdup profiles at different axial locations during periodic flow modulation.

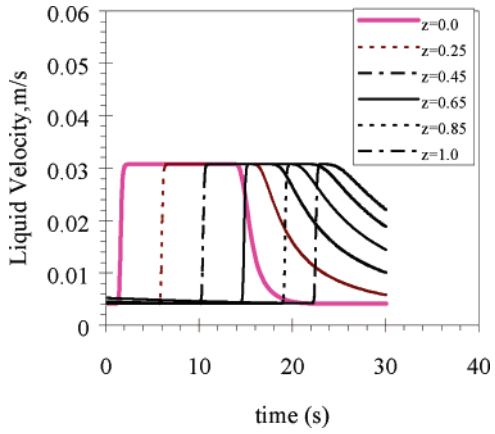

Figure 3. Transient liquid velocity profiles at different axial locations during periodic flow modulation.

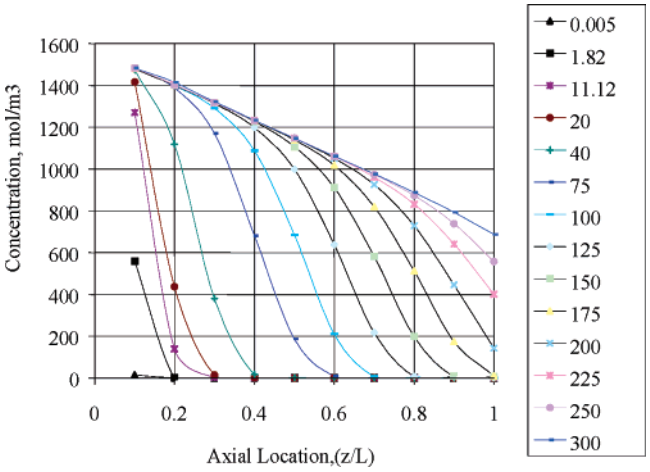

Figure 4. α-Methylstyrene concentration profile development with time (shown in seconds in the legend table).

concentrations drop below saturation concentration (14 mol/m^3) as the liquid reactant reaches each downstream location in the reactor. This behavior of the reactant concentration is observed during the ON part of each cycle or during a pseudotransient operation simulation to steady state. In full cycle simulations, the reactant flow would be modulated after the initial ON part and the catalyst would see the effects of both parts of the cycle as discussed next.

Periodic Flow Modulation: Full Cycle Reaction Transport Simulation. Several test case simulations were conducted with flow modulation to demonstrate

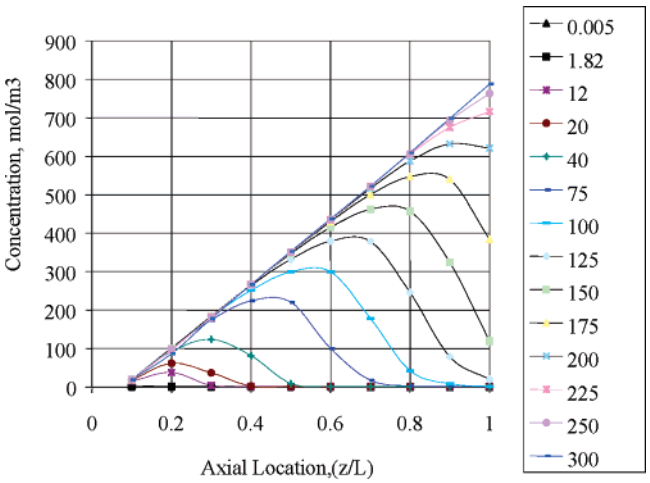

Figure 5. Axial profiles of cumene concentration at different times (shown in the legend table in seconds).

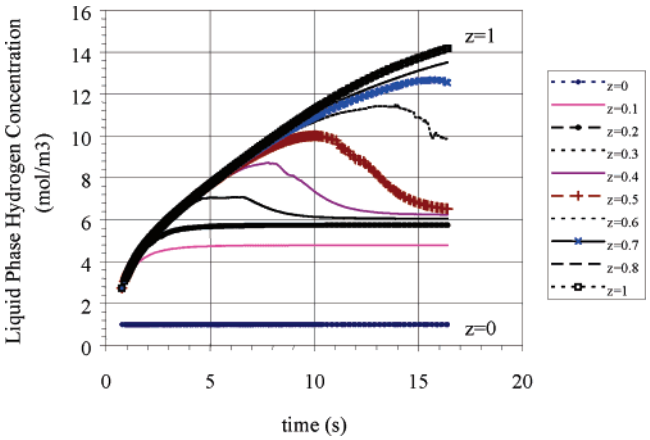

Figure 6. Transient hydrogen concentration profiles at different axial locations.

the effect of unsteady state operation on species concentration and hence the performance of the trickle bed. Results of one such test case are presented here to show the effects of flow modulation on reactant and product concentrations over one cycle period. The liquid reactant (α-methylstyrene) feed concentration is 1484 mol/m^3, and mass velocity is 0.21 kg/(m^2 s) (corresponding to an interstitial liquid velocity of 0.009 m/s and feed holdup of 0.03211). The gas superficial velocity used was 0.038 m/s at 1 atm operating pressure. The total cycle period (τ) chosen for this case is 60 s with a liquid ON time of 20 s (or a cycle split (σ) of 0.33).

Figure 7 shows supply of α-methylstyrene to a previously dry pellet during the liquid ON part of the cycle (0−20 s). This is followed by consumption of the α-methylstyrene by enhanced supply of hydrogen during the liquid OFF part of the cycle (20−60 s). The figure also shows that high α-methylstyrene concentrations are possible at downstream locations during some part of the cycle under unsteady state conditions, which would not be possible in steady state operation. Production rates of cumene are shown in Figure 8 during the same cycle in the same previously dry pellet at different axial locations. During the ON part of the cycle (0−20 s), cumene production is small due to lower gaseous reactant supply to the pellet, which is followed by high production rates corresponding to enhanced supply of hydrogen to the pellet during the OFF cycle. This also demonstrates the lessening of the gaseous reactant limitation due to periodic liquid flow modulation.

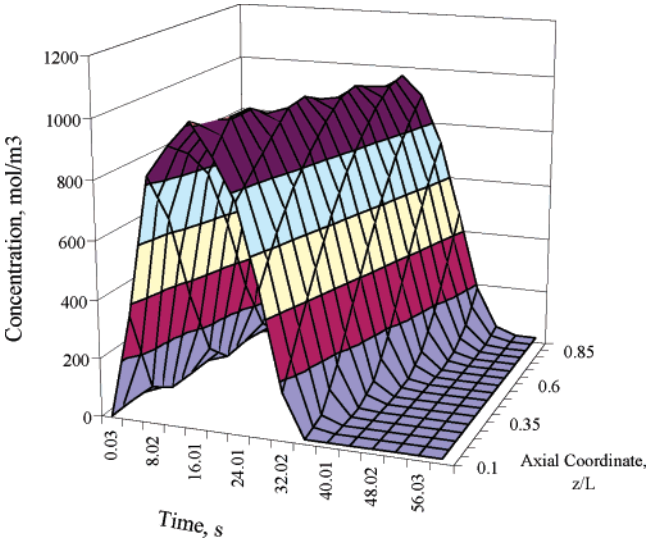

Figure 7. Intracatalyst α-methylstyrene concentration profiles during flow modulation for a previously externally dry pellet at different axial locations.

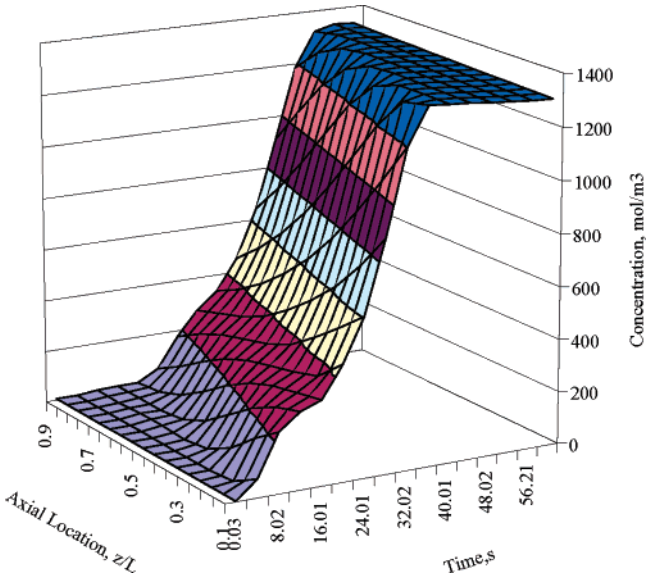

Figure 8. Intracatalyst cumene concentration profiles during periodic flow modulation.

The supply of hydrogen to the catalyst pellet is not easy to illustrate due to its complete consumption as the limiting reactant. Hence, this is shown in Figure 9 for a pellet in which reaction rates are deliberately set to be very low. The hydrogen concentration profile at the beginning of the cycle shows a low concentration (~3.5 mol/m^3) in the pellet. This is followed by significantly higher supply of hydrogen during the OFF part of the cycle, enhancing the reaction rate further, which is reflected in the higher cumene concentration (as shown in Figure 8). Bulk cumene concentration profiles also corroborate the enhanced rate as for the same set of conditions. Cumene concentrations should however not be directly used in comparison with the steady state profiles since the holdup and velocity changes need to be accounted for in the unsteady state performance evaluation. Proper comparison requires the evaluation of flow averaged conversion or of time averaged reaction rate at each point in the reactor, which can then be used to obtain an overall rate (for the cycle) in the entire

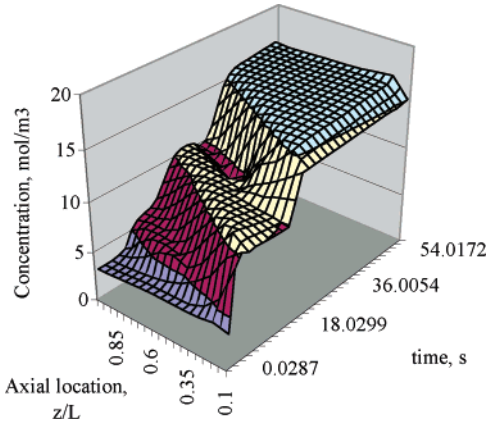

Figure 9. Intracatalyst hydrogen concentration for a negligible reaction test case.

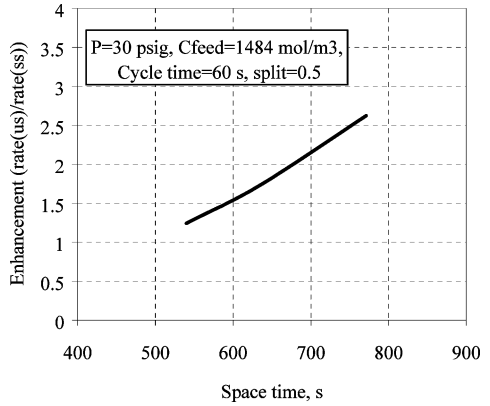

Figure 10. Effect of mean liquid flow (space time) on simulated unsteady state performance (for experimental data see Khadilkar et al.[48]).

reactor. The latter approach is used in comparison of simulated reaction rates with steady state reaction rates.

Effects of Cycling Parameters on Performance. The above test case simulations demonstrate the capability of the model to effectively capture the transient behavior in terms of flow variables (velocity and holdup) and reaction and transport of limiting and nonlimiting species. The model is now used to compare the reactor performance under unsteady state conditions to that under steady state. Three key parameters associated with periodic flow modulation operation are flow amplitude (inverse space-time), total cycle time, and cycle split (fraction of the cycle with liquid flow ON). The effect of these on reactor performance determines the optimum operating conditions for unsteady state operation. Since we are primarily interested in performance enhancement over steady state, the reaction rate constant is set arbitrarily and only an estimate of enhancement is compared in all the simulations presented here. Figure 10 shows the effect of flow modulation amplitude (in terms of nominal space-time corresponding to mean liquid mass velocity) on the performance enhancement under gas limited conditions at 30 psig operating pressure and feed concentration of 1484 mol/m^3. This figure shows higher enhancement at higher space-time, which is in agreement with experimental observations.[6,10,48] The reduction in catalyst external wetting at higher space-time (lower mean liquid mass velocity) allows enhanced supply of the gaseous reactant and results in the reduction of gaseous reactant limitation and correspondingly higher enhancement over steady

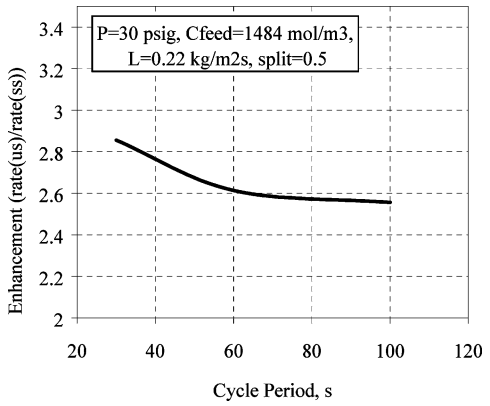

Figure 11. Effect of total cycle time on simulated unsteady state performance (for experimental data see Khadilkar et al.[48]).

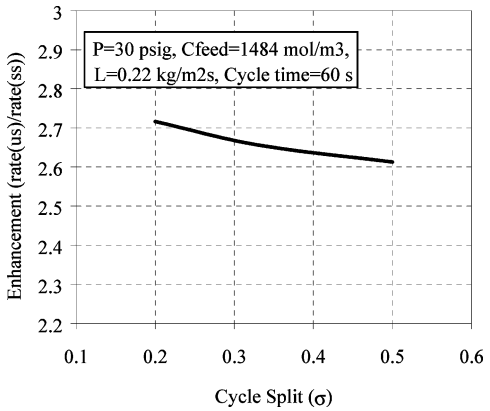

Figure 12. Effect of cycle split on simulated unsteady state performance (for experimental data see Khadilkar et al.[48]).

state performance. The exact quantitative comparison between these simulations and the experimentally observed enhancement was not pursued here due to the uncertainty in the exact prediction of several factors such as catalyst wetting, dynamics of transport coefficients, thermal effects, assumptions in the apparent rate model, and hydrodynamic parameters evaluated under dynamic conditions.

Figure 11 shows the total cycle period dependence of the simulated rate under gas limited operating conditions (P = 30 psig, α-methylstyrene concentration = 1484 mol/m^3, cycle split = 0.5). The rate enhancement (which is about 100%) is seen to decrease slightly with increase in cycle time, indicating that the extent of liquid reactant starvation close to externally dry pellet areas increases with the increase in total cycle time as was observed in experimental studies.[5,48] The other extreme that was observed in experiments, at which gaseous reactant starvation causes a decrease in performance, is not seen here for the range of cycle times simulated. As discussed above, the exact point at which the maximum enhancement and shift to gaseous reactant starvation can be observed depends on the accuracy of the prediction of the dynamic variation of transport parameters. At much lower cycle times, such a decrease in enhancement can be expected due to frequent supply of liquid reactants and inadequate time for gaseous reactant supply for complete consumption of the accumulated liquid reactant resulting in enhanced gas limitation. Hence, a complete enhancement feasibility envelope observed experimentally[7,48] is not captured in the range of the cycle times simulated.

The influence of cycle split (fraction of the cycle with liquid ON) was simulated by setting the same mean flow and varying the liquid ON time to obtain cycle splits of 0.5, 0.33, and 0.2. The simulated unsteady state performance shows the expected trend in performance enhancement, i.e., increase in enhancement with a decrease in cycle split (Figure 12). This was also observed experimentally[5,6,48] and explained on the basis of enhanced gaseous reactant access to the catalyst during the liquid OFF time. The extent of enhancement observed is not quantitatively comparable to the experimental enhancement due to factors discussed earlier. The simulation is, however, able to capture the broad trends in the experimentally observed data. Further refinements in the estimation of transport parameters should be able to improve the match with the experimentally observed enhancement quantitatively. It must be noted that only a 1-D model is used here for demonstration of the key phenomena observed experimentally. Accurate prediction of the flow distribution by 2-D and 3-D models using fluid dynamic codes should allow better match with the experimental data. This is also the reason why liquid limited operation was not simulated by this model, since liquid limited conditions require finer resolution of the external partial wetting than obtained by a three-pellet representation. A 2-D representation of flow[11,53,54] is warranted for such predominantly wetting driven enhancement under liquid limited conditions.

Summary and Conclusions

A reactor and pellet scale flow-transport-reaction model using multicomponent Stefan−Maxwell formulation was developed to simulate unsteady state operation in trickle bed reactors. This model eliminates several simplifications and shortcomings of previous models and was demonstrated to be particularly suitable for simulating dynamic variation of phase holdups and velocities, as well as simulating the transport of all reacting and nonreacting species and resulting interaction between flow, reaction, and transport. The developed model was tested successfully on simulation of periodic liquid flow modulation (under gas reactant limited conditions) to demonstrate its capability in describing the dynamic access of gaseous and liquid reactants and performance enhancement under these conditions. Reactor performance enhancement was shown to increase with decrease in mean liquid flow, total cycle period, and cycle split. The simulated results are in qualitative agreement with those reported in the literature. Extension of the model to a multidimensional computational fluid dynamics (CFD) based model is required for better match with experimental results reported in the literature.

Notation

a = interfacial area per unit volume of reactor
$[B]$ = mass transfer coefficient matrix
C = concentration
D = diffusivity
d_t = reactor diameter
d_p = catalyst pellet diameter
E = energy transfer flux
F_d = liquid−solid drag
g = gravitational acceleration
H = enthalpy
h = heat transfer coefficient

k = mass transfer coefficient
K = equilibrium constant
K = interphase momentum transfer coefficient
l = film thickness
L = length
M = molecular weight of species i
nc = number of components
N = flux at the interface
p = pressure
q = heat flux
R = reaction rate
T = temperature
u_I = interstitial (actual) velocity
x = mole fraction in the liquid phase
y = mole fraction in the gas phase
z = axial coordinate
zc = intrapellet spatial coordinate

Greek Symbols

α = intermediate velocity correction coefficient
β = intermediate velocity correction coefficient
$[\beta]$ = bootstrap matrix in Maxwell−Stefan formulation
$[\Gamma]$ = activity correlation matrix
ϵ = phase holdup
ν = stoichiometric coefficient of component
ρ = density
η_{CE} = contacting efficiency
λ_x = latent heat
$[\Lambda]$ = latent heat matrix
$[\Phi]$ = flux correction matrix
ω = pressure equation coefficient
σ = cycle split
τ = cycle period

Subscripts and Superscripts

A = ambient
A,B,C = components
B = bed voidage
C = catalyst
G = gas phase
I = interface
i,j,k = species number
L = liquid phase
S = solid phase
t = total
V = vapor
W = wet

Appendix A. Derivation of Multicomponent Transport Matrices: Key Equations

This appendix illustrates the equations needed for the solution of simultaneous mass and energy transfer fluxes at the gas−liquid interface listed in Table 3. An analogous procedure can be followed to formulate equations for the gas−solid and liquid solid interfaces as listed in Table 4.

For a system with nc components, the number of unknowns is 2(nc) mole fractions at the interface (x_i^I and y_i^I), nc molar fluxes (incorporating $N_i^L = N_i^V = N_i^{VL}$), and an interface temperature (T^I). Since thermal energy balance at the interface is also considered, it acts as a bootstrap to relate the total flux to the absolute quantities without needing any further assumptions (such as of inert flux being zero or stoichiometric fluxes of reacting species etc.). Thus the total number of variables is 3(nc) + 1. The number of equations that relate these variables is as follows.

(a) nc − 1 rate equations for the liquid phase given by

$$N_i^L = J_i^L - x_i \sum_{k=1}^{n-1} \Lambda_{ik} J_k^L + x_i \frac{\Delta q}{\lambda_x} \tag{A1}$$

where

$$(J^L) = c_t^L [k_L^\bullet](x^I - x^L) \tag{A2}$$

and

$$\Lambda_{ik} = (\lambda_k - \lambda_n)/\lambda_x,$$

$$\Delta q = h_L^\bullet (T_I - T_L) - h_V^\bullet (T_G - T_I), \tag{A3}$$

$$\lambda_x = \sum_{i=1}^{n} \lambda_i x_i$$

where

$$\lambda_i = \overline{H_i^V} - \overline{H_i^L} \tag{A4}$$

(b) nc − 1 rate equations for the vapor(gas) phase given by

$$N_i^V = J_i^V - y_i \sum_{k=1}^{n-1} \Lambda_{ik} J_k^V + y_i \frac{\Delta q}{\lambda_y} \tag{A5}$$

where

$$(J^V) = c_t^V [k_V^\bullet](y^V - y^I) \quad \text{and} \quad \lambda_y = \sum_{i=1}^{n} \lambda_i y_i \tag{A6}$$

(c) nc equilibrium relations:

$$y_i^I = K_i(x_i^I, y_i^I, T_I) x_i^I \tag{A7}$$

(d) Interfacial energy balance:

$$h_L^\bullet (T_I - T_L) + \sum_{i=1}^{n} N_i^L \overline{H_i^L}(T_L) = h_V^\bullet (T_G - T_I) + \sum_{i=1}^{n} N_i^V \overline{H_i^V}(T_G) \tag{A8}$$

(e) Two more equations are necessary to complete the set and are given by the mole fraction sum for both gas and liquid compositions at the interface.

$$\sum x_i^I = 1 \tag{A9}$$

$$\sum y_i^I = 1 \tag{A10}$$

The "Bootstrap" Matrix for Interphase Transport. Note that eqs A1 and A5 are written for only nc − 1 components since they are based on relative fluxes (eqs A2 and A6) and hence are governed by the Gibbs−Duhem restriction, which allows definition of only nc − 1 equations for an nc component system. The extra condition required for the complete definition of the set of equations is commonly referred to as the "bootstrap" condition. The entire set of transport equations including the bootstrap condition can then be formulated in terms of a bootstrap matrix $[\beta]$ which can be incorporated in the flux evaluation. For the gas side of the gas−liquid transport, the bootstrap condition is based on the interphase energy transfer flux at the gas−liquid in-

terface:

$$[\beta_{i,k}]_G = \delta_{ik} - y_i \Lambda_{ik} \quad \text{(A11)}$$

where

$$\Lambda_{ik} = (\lambda_k - \lambda_{nc})/\lambda_y \quad \text{(A12)}$$

$$\lambda_y = \sum_i y_i \lambda_i, \qquad \lambda_i = y_i(H_i^V(@T_G) - H_i^L(@T_L)) \quad \text{(A13)}$$

The bootstrap matrix for the liquid phase of the gas−liquid transport is also based on the energy flux term and given by

$$[\beta_{i,k}]_L = \delta_{ik} - x_i \Lambda_{ik} \quad \text{(A14)}$$

where

$$\Lambda_{ik} = (\lambda_k - \lambda_{nc})/\lambda_x \quad \text{(A15)}$$

$$\lambda_x = \sum_i x_i \lambda_i, \qquad \lambda_i = x_i(H_i^V(@T_G) - H_i^L(@T_L)) \quad \text{(A16)}$$

Mass Transfer Coefficient: Matrix Form. The expressions for the mass transfer fluxes can be written in terms of the mass transfer coefficients (k_{ij}), which are estimated from the binary diffusivities (D_{ij} estimated using correlations in Table 8) as shown below.

(a) For the gas side of the gas−liquid interface, the low flux mass transfer coefficient matrix can be calculated as

$$[k]_G = [B]^{-1}[\Gamma] \quad \text{(A17)}$$

where

$$[B_{i,j}] = \frac{y_i}{k_{i,nc}} + \sum_k \frac{y_k}{k_{i,k}} \quad (\text{for } i = j) \quad \text{(A18)}$$

$$[B_{i,j}] = -y_i\left(\frac{1}{k_{i,j}} - \frac{1}{k_{i,nc}}\right) \quad (\text{for } i \neq j) \quad \text{(A19)}$$

Here $[k_{i,j}] = D_{i,j}/l$ where the diffusivity coefficients are calculated from kinetic theory and the film thickness, l, is calculated from Sherwood number correlations listed in Table 8.

The nonideality coefficient matrix, [Γ], consisting of the elements $d(\ln \gamma_i)/dx_i$ is considered to be the identity matrix for the gas side.

(b) The liquid side gas−liquid mass transfer coefficient matrix is calculated similarly as

$$[k]_L = [B]^{-1}[\Gamma] \quad \text{(A20)}$$

where

$$[B_{i,j}] = \frac{y_i}{k_{i,nc}} + \sum_k \frac{y_k}{k_{i,k}} \quad (\text{for } i = j) \quad \text{(A21)}$$

$$[B_{i,j}] = -y_i\left(\frac{1}{k_{i,j}} - \frac{1}{k_{i,nc}}\right) \quad (\text{for } i \neq j) \quad \text{(A22)}$$

Here $[k_{i,j}] = D_{i,j}/l$ where the diffusivity coefficients are calculated from infinite dilution theory using mole fraction weighting factors as shown in Table 8. The nonideality coefficient matrix, [Γ], for liquid phase is determined from the activity coefficient models such as Wilson's, Van-Laar's, UNIFAC, etc., as given by Taylor and Krishna.[28]

High Flux Correction. The mass transfer coefficients determined above are valid at very low flux limits and need to be corrected for high fluxes, which is particularly important for the gas side mass transfer coefficients as the on period for liquid during periodic operation is reached. This high flux correction can be determined as below.

Determine the flux corrector matrix [Φ] based on the first pass calculated fluxes evaluated from low flux transport coefficients.

$$\Phi_{ij} = \frac{N_i}{c_t k_{in}} + \sum \frac{N_k}{c_t k_{ik}} \quad (\text{for } i = j) \quad \text{(A23)}$$

$$\Phi_{ij} = -N_i\left(\frac{1}{c_t k_{ij}} - \frac{1}{c_t k_{in}}\right) \quad (\text{for } i = j) \quad \text{(A24)}$$

Correct the low flux mass transfer coefficient matrix by the following equation:

$$[k]_{highflux} = [k]_{lowflux}[\Phi][\exp([\Phi]) - [I]]^{-1} \quad \text{(A25)}$$

where $\exp([\Phi])$ is evaluated by a Pade approximation[30] as

$$\exp([\Phi]) = \{[I] + [\Phi]/2\} - \{[I] - [\Phi]/2\} \quad \text{(A26)}$$

Similarly, the heat transfer coefficient determined using a low flux correlation (as listed in Table 8) is also corrected by calculating the flux correction factor Φ and then using it to correct the low flux heat transfer coefficient as

$$\Phi_{ht} = \frac{\sum N_i C_{pi}}{h} \quad \text{(A27)}$$

$$h_{highflux} = h_{lowflux}\Phi_{ht}/(\exp(\Phi_{ht}) - 1) \quad \text{(A28)}$$

Appendix B. Solution of Momentum and Continuity Equations

This appendix describes a three-step procedure for solving the momentum and continuity equations of the model. The procedure below assumes that velocity, holdup, and pressure are known at all axial locations at the current time instant.

Step 1. Evaluation of Intermediate Calculated Phase Velocity. The momentum equation is evaluated explicitly (at the nth time instant) to obtain an estimate of the velocities at the next ($(n + 1)$th) time instant. Since these velocities will not satisfy continuity, they are considered only as intermediate values for further calculations. The phase holdups and pressure used here are also the nth level values to be updated subsequently.

$$\epsilon_L \rho_L u_{iL}^* = \epsilon_L \rho_L u_{iL}^n + \Delta t\left(-\epsilon_L \rho_L u_{iL}^n \frac{\partial u_{iL}^n}{\partial z} + \epsilon_L \rho_L g - \epsilon_L \frac{\partial p^n}{\partial z} - F_{D,Liq}^n + K(u_{iG}^n - u_{iL}^n)\right) \quad \text{(B1)}$$

$$\epsilon_G\rho_G u^*_{iG} = \epsilon_G\rho_G u^n_{iG} + \Delta t\left(-\epsilon_G\rho_G u^n_{iG}\frac{\partial u^n_{iG}}{\partial z} + \epsilon_G\rho_G g - \epsilon_G\frac{\partial p^n}{\partial z} - F^n_{D,Gas} - K(u^n_{iG} - u^n_{iL})\right) \quad \text{(B2)}$$

Similarly, we write implicit equations for the phase velocities at the next time instant with all the terms evaluated implicitly. Subtracting the above eqs B1 and B2 from the implicit equations, we get a relationship between the intermediate values and the new actual velocity values (at the $(n + 1)$th time step) as follows.

$$\epsilon_L\rho_L u^{n+1}_{IL} = \epsilon_L\rho_L u^*_{IL} + \Delta t\left(-\epsilon_L\frac{\partial(p^{n+1} - p^n)}{\partial z} + K((u^{n+1}_{IG} - u^*_{IG}) - (u^{n+1}_{IL} - u^*_{IL}))\right) \quad \text{(B3)}$$

$$\epsilon_G\rho_G u^{n+1}_{IG} = \epsilon_G\rho_G u^*_{IG} + \Delta t\left(-\epsilon_G\frac{\partial(p^{n+1} - p^n)}{\partial z} - K((u^{n+1}_{IG} - u^*_{IG}) - (u^{n+1}_{IL} - u^*_{IL}))\right) \quad \text{(B4)}$$

Step 2. Evaluation of the Pressure over the Domain. In order to calculate the pressure at the next time step, we eliminate the velocities of the gas and liquid at the next time instant $(n + 1)$. This is done by substituting the above eqs B3 and B4 into the continuity equations (eqs 6 and 7 in manuscript) (and eliminating the time derivatives by addition) to obtain the Poisson equation for pressure as shown below.

This is done differently for the following two cases:

(a) Constant Density (Volume Fraction Addition) Method. This is done in two stages. First the right-hand side of eqs B3 and B4 is simplified to separate the nonprimary intermediate variables (u^*_{IG} in the equation for the liquid and u^*_{IL} in equation for the gas), and to get

$$u^{n+1}_{IL} = u^*_{IL} - \Delta t\left(\frac{(1-\alpha)}{\rho_L} + \frac{\alpha}{\rho_G}\right)\frac{\partial(\delta p)}{\partial z} \quad \text{(B5)}$$

$$u^{n+1}_{IG} = u^*_{IG} - \Delta t\left(\frac{(1-\beta)}{\rho_G} + \frac{\beta}{\rho_L}\right)\frac{\partial(\delta p)}{\partial z} \quad \text{(B6)}$$

where

$$\delta p = p^{n+1} - p^n \quad \text{(B7)}$$

and

$$\alpha = K\rho_G\epsilon_G\Delta t/(\rho_G\epsilon_G\rho_L\epsilon_L + (\rho_L\epsilon_L + \rho_G\epsilon_G)K\Delta t) \quad \text{(B8)}$$

$$\beta = K\rho_L\epsilon_L\Delta t/(\rho_L\epsilon_L\rho_G\epsilon_G + (\rho_L\epsilon_L + \rho_G\epsilon_G)K\Delta t) \quad \text{(B9)}$$

Substituting these in the continuity equation of the appropriate phase and eliminating the $(n + 1)$th level velocities of the gas and liquid yields

$$\sum N^{GL}_i a_{GL} M_i\left(\frac{1}{\rho_G} - \frac{1}{\rho_L}\right) + \sum\frac{N^{GS}_i a_{GS} M_i}{\rho_G} + \sum\frac{N^{LS}_i a_{LS} M_i}{\rho_L} + \frac{\partial(\epsilon_L u^*_{IL})}{\partial z} + \frac{\partial(\epsilon_L u^*_{IL})}{\partial z} = \Delta t\frac{\partial}{\partial z}\left(\omega\frac{\partial(\delta p)}{\partial z}\right) \quad \text{(B10)}$$

where

$$\omega = \epsilon_L\left(\frac{1-\alpha}{\rho_L} - \frac{\alpha}{\rho_G}\right) + \epsilon_G\left(\frac{1-\beta}{\rho_G} - \frac{\beta}{\rho_L}\right) \quad \text{(B11)}$$

This is the familiar Poisson equation for pressure, written here in terms of the pressure difference in time ($\delta p = p^{n+1} - p^n$). This equation has to be solved for the entire spatial domain and can be arranged in the form of a tridiagonal matrix when assembled for all spatial locations. The boundary conditions for pressure used are that the pressure gradients in time (δp) just outside the inlet and the exit are zero based on the physics of the problem. It must be noted here that the pressure values are evaluated at the center of the grid over which the velocity is calculated. The tridiagonal system of equations is then solved efficiently by the Thomas algorithm.[43]

(b) Variable Density Correction (Rigorous Algorithm). Here eqs B3 and B4 are substituted in their respective continuity equations by premultiplying them with the corresponding density and phase holdups. Equation B12 is then obtained by elimination of the time derivatives of holdup (which get eliminated on summation of the continuity equations) as

$$\sum N^{GL}_i a_{GL} M_i\left(\frac{1}{\rho_G} - \frac{1}{\rho_L}\right) + \sum\frac{N^{GS}_i a_{GS} M_i}{\rho_G} + \sum\frac{N^{LS}_i a_{LS} M_i}{\rho_L} + \frac{1}{\rho_L}\frac{\partial(\rho_L\epsilon_L u^*_{IL})}{\partial z} + \frac{1}{\rho_G}\frac{\partial(\rho_G\epsilon_G u^*_{IG})}{\partial z} + \epsilon_L\frac{\partial \ln \rho_L}{\partial t} + \epsilon_G\frac{\partial \ln \rho_G}{\partial t} = \Delta t\left[\frac{1}{\rho_L}\frac{\partial}{\partial z}\left(\omega_L\frac{\partial(\delta p)}{\partial z}\right) + \frac{1}{\rho_G}\frac{\partial}{\partial z}\left(\omega_G\frac{\partial(\delta p)}{\partial z}\right)\right] \quad \text{(B12)}$$

where

$$\omega_L = \rho_L\epsilon_L\left(\frac{1-\alpha}{\rho_L} - \frac{\alpha}{\rho_G}\right)$$

and

$$\omega_G = \rho_G\epsilon_G\left(\frac{1-\beta}{\rho_G} - \frac{\beta}{\rho_L}\right) \quad \text{(B13)}$$

Here the derivatives of density may be neglected for simplicity.

The choice of the method to be used depends typically on the extent of interphase mass transfer fluxes as a result of evaporation, condensation, etc. When interfacial mass transfer fluxes are small ($<10^{-3}$ mol/(m^2 s)), the first method is used. For cases where the transferred

flux can affect the density of the phases (particularly the gas phase), the second method is more appropriate and is recommended. If, however, the extent of interfacial transport and phase change is very large, a compressible version based on a combined phase equation of state is recommended.

Step 3. Update and Holdup Evaluation. The pressure obtained from the solution of the above set of eqs B10 or B12 is used to update the velocities (using eqs B5 and B6 for the $(n + 1)$th time instant). These velocities are in turn used to update holdup at the next instant using the continuity equations as

$$\rho_L \epsilon_L^{n+1} = \rho_L \epsilon_L^n + \Delta t\left(\frac{\partial(\rho_L u_{IL} \epsilon_L)}{\partial z} + \sum N_i^{GL} a_{GL} M_i - \sum N_i^{LS} a_{LS} M_i\right) \quad \text{(B14)}$$

$$\rho_G \epsilon_G^{n+1} = \rho_G \epsilon_G^n + \Delta t\left(\frac{\partial(\rho_G u_{IG} \epsilon_G)}{\partial z} - \sum N_i^{GL} a_{GL} M_i - \sum N_i^{GS} a_{GS} M_i\right) \quad \text{(B15)}$$

This procedure for pressure calculation and velocity correction is continued until velocities and pressures converge to a set tolerance. Adaptive time halving is used to ensure accuracy and stability of the flow solution (required due to the explicit part of the procedure). Liquid holdup and liquid and gas velocity profiles over the entire reactor length are calculated at a full time step and two-half time steps and compared to check for convergence.

Literature Cited

(1) Dudukovic, M. P.; Larachi, F.; Mills, P. L. Multiphase Reactors Revisited *Chem. Eng. Sci.* **1999**, *54*, 1975−1995.

(2) Al-Dahhan, M. H.; Larachi, F.; Dudukovic, M. P.; Laurent, A. High-Pressure Trickle Bed Reactors: A Review. *Ind. Eng. Chem. Res.* **1997**, *36* (8), 3292.

(3) Saroha, A. K.; Nigam, K. D. P. Trickle Bed Reactors. *Rev. Chem. Eng.* **1996**, *12*, 207.

(4) Silveston, P. In *Unsteady State Processes Catal., Proc. Int. Conf.* **1990**, 217−232.

(5) Haure, P. M.; Bogdashev, S. M.; Bunimovich, M.; Stegasov, A. N.; Hudgins, R. R.; Silveston, P. L. Thermal Waves in Periodic Operation of Trickle Bed Reactor. *Chem. Eng. Sci.* **1990**, *45*, 2255.

(6) Lange, R.; Hanika, J.; Stradiotto, D.; Hudgins, R. R.; Silveston, P. L. Investigations of Periodically operated Trickle-bed Reactors. *Chem. Eng. Sci.* **1994**, *49*, 5615.

(7) Castellari, A.; Haure, P. M. Experimental Study of the Periodic Operation of a Trickle-bed Reactor. *AIChE J.* **1995**, *41*, 1593.

(8) Lee, J. K.; Hudgins, R. R.; Silveston, P. L. Cycled Trickle Bed Reactor for SO2 Oxidation. *Chem. Eng. Sci.* **1995**, *50*, 2523.

(9) Stradiotto, D. A.; Hudgins, R. R.; Silveston P. L. Hydrogenation of crotonaldehyde under periodic flow interruption in a trickle bed. *Chem. Eng. Sci.* **1999**, *54*, 13−14.

(10) Khadilkar, M. R.; Al-Dahhan, M.; Duduković, M. P Simulation of Unsteady State Operation of Trickle Bed Reactors. AIChE Annual Meeting, Los Angeles, CA, 1997, Presentation 254e.

(11) Khadilkar, M. R. Performance Studies of Trickle Bed Reactors. D.Sc. Dissertation, Washington University, St. Louis, MO, 1998.

(12) Lange, R.; Gutsche R.; Hanika, J. Forced Periodic Operation of a Trickle-Bed Reactor. *Chem. Eng. Sci.* **1999**, *54* (13−14), 2569−2573.

(13) Lange, R. Zur Stationaeren und Periodschen Betriebsweise von Trickle-Bed Reactoren′. Habilitation Thesis, Technical University of Hamburg-Harburg, Germany 2001.

(14) Hanika, J.; Lange, R. Dynamic aspects of adiabatic trickle bed reactor control near the boiling point of reaction mixture. *Chem. Eng. Sci.* **1996**, *51*, 11.

(15) Giakoumakis, D.; Kostoglou, M.; Karabelas, A. J. Induced Pulsing Flow in Trickle-Beds: Characteristics and Attenuation of Pulses. Presented at the 3rd European Conference on Chemical Engineering, Nuremberg, Germany, 2001.

(16) Schubert, S.; Grunewald, M.; Lange, R. Dynamic Modeling and Simulation of Trickle-Bed Reactors Underlying Operation Mode. Presented at the 4th European Congress on Chemical Engineering, Granada, Spain, 2003.

(17) Yan, T. Y. Dynamics of a Trickle Bed Hydrocracker with a Quenching System. *Can. J. Chem. Eng.* **1980**, *58*, 259.

(18) Stegasov, A. N.; Kirillov, V. A.; Silveston, P. L. Modeling of Catalytic SO_2 Oxidation for Continuous and Periodic Liquid Flow Through a Trickle Bed. *Chem. Eng. Sci.* **1994**, *49*, 3699.

(19) Wu R.; McReady, M. J.; Varma, A. Influence of Mass Transfer Coefficient Fluctuation Frequency on Performance of Three-Phase Packed Bed Reactors. *Chem. Eng. Sci*. **1995**, *50*, 3333.

(20) Warna, J.; Salmi, T. Dynamic Modeling of Three Phase Reactors. *Comput. Chem. Eng.* **1996**, *20*, 39.

(21) Yamada, H.; Goto, S. Periodic Operation of Trickle Bed Reactor for Hydrogenolysis in Gas-Liquid-Liquid-Solid Four Phases. *J. Chem. Eng. Jpn.* **1997**, *30*, 478.

(22) Gabarain, L.; Castellari, A. T.; Cechini, J.; Tobolski, A.; Haure, P. Analysis of Rate Enhancement in a Periodically Operated Trickle-bed Reactor. **1997**, *43*, 166.

(23) Lange, R.; Schubert, W.; Dietrich, M.; Grunewald, M. Unsteady State Operation of Trickle-Bed Reactors. ISCRE 18, Chicago, IL, June 6−9, 2004.

(24) Harold, M. P.; Watson, P. C. Bimolecular Exothermic Reaction with Vaporization in the Half-wetted Slab Catalyst. *Chem. Eng. Sci.* **1993**, *48*, 981.

(25) Khadilkar, M. R.; Mills, P. L.; Duduković, M. P. Trickle Bed Reactor Models for Systems with Volatile Liquids. *Chem. Eng. Sci.* **1999**, 54.

(26) Attou, A.; Boyer, C.; Ferschneider, G. Modeling of the hydrodynamics of the cocurrent gas-liquid trickle flow through a trickle-bed reactor, *Chem. Eng. Sci.* **1999**, *54*, 785−802.

(27) Holub, R. A.; Dudukovic, M. P.; Ramachandran, P. A. Pressure Drop, Liquid Holdup and Flow Regime Transition in Trickle Flow. *AIChE J*. **1993**, *39*, 302.

(28) Taylor, R.; Krishna, R. *Multicomponent Mass Transfer*; John Wiley and Sons Inc.: New York, 1993.

(29) Krishna, R. Problems and Pitfalls in the use of Fick Formulation for Intraparticle Diffusion. *Chem. Eng. Sci.* **1993**, *48*, 845.

(30) Toppinen, S.; Aittamaa, J.; Salmi, T. Interfacial Mass Transfer in Trickle-Bed Reactor Modeling. *Chem. Eng. Sci.* **1996**, *51*, 4335.

(31) Beaudry, E. G.; Dudukovic, M. P.; Mills, P. L. Trickle Bed Reactors: Liquid Diffusional Effects in a Gas Limited Reaction.′ *AIChE J.* **1987**, *33*, 1435.

(32) Jaguste, D. N.; Bhatia, S. K. Partial Internal Wetting of Catalyst Particles: Hysteresis Effects. *AIChE J.* **1991**, *37*, 661−670.

(33) Khadilkar, M. R.; Wu, Y.; Al-Dahhan, M.; Duduković, M. H.; Colakyan, M. Comparison of Trickle-Bed and Upflow Reactor Performance at High Pressure: Model Predictions and Experimental Observations. *Chem. Eng. Sci.* **1996**, *51* (10), 2139.

(34) El-Hisnawi, A. A.; Dudukovic, M. P.; Mills P. L. Trickle Bed Reactors: Dynamic Tracer Tests, Reaction Studies, and Modeling Reactor Performance. *ACS Symp. Ser.* **1982**, *196*, 421−440.

(35) Al-Dahhan, M. H.; Dudukovic, M. P. Catalyst Wetting Efficiency in Trickle Bed Reactors at High Pressure. *Chem. Eng. Sci.* **1995**, *50*, 2377−2389.

(36) Villadsen, J. V.; Michelsen, M. L. *Solution of Differential Equation Models by Polynomial Approximation*; Prentice Hall: Englewood Cliffs, NJ, 1978.

(37) Finlayson, B. *Numerical Methods for Problems with Moving Fronts*; Ravenna Park Publishing Inc.: 1992.

(38) Gardini, L.; Servida, A.; Morbidelli, M.; Carra, S. Use of Orthogonal Collocation on Finite Elements with Moving Boundaries for Fixed Bed Catalytic Reactor Simulation. *Comput. Chem. Eng.* **1985**, *9*, 1.

(39) Hindmarsh, A. C. ODEPACK, A Systematatized Collection of ODE Solvers. In *Scientific Computing*; Stepleman, R. S., Ed.; North-Holland: Amsterdam, 1983.

(40) Petzold, L. R. A Description of DASSL: A Differential/Algebraic System Solver. In *Proceedings of IMACS World Congress*, Montreal, Canada, August 1982; p 65.

(41) Madsen, N. K.; Sincovec, R. F. PDECOL, A General Collocation Software for Partial Differential Equations. *ACM Trans. Math. Software* **1980**, *5*, 326.

(42) Oh, M.; Pantelides, C. C. A Modeling and Simulation Language for Combined Lumped and Distributed Parameter Systems. *Comput. Chem. Eng.* **1995**.

(43) Press, W. H.; Teukolsky, S. A.; Vetterling, W.; Flannery, B. P. *Numerical Recipes in Fortran*; Cambridge University Press: New York, 1992.

(44) Welch, J. Eddie; Harlow, Francis H.; Shannon, John, P.; Daly, Bart J. *MAC [Marker-and-cell] Method—Computing Technique for Solving Viscous, Incompressible, Transient Fluid-Flow Problems involving Free Surfaces*; Los Alamos Sci. Lab.: Los Alamos, NM, 1965.

(45) Anderson, D. A.; Tannenhill, J. C.; Pletcher, R. H. *Computational Fluid Mechanics and Heat Transfer*; Hemisphere Publishing Company: Bristol, PA, 1984.

(46) Versteeg, H. K.; Malalasekera, W. *An Introduction to Computational Fluid Dynamics: The Finite Volume Method*; Longman Scientific and Technical: Essex, U.K., 1995.

(47) Patankar, S. V. *Numerical Heat Transfer and Fluid Flow*; McGraw-Hill: New York, 1980.

(48) Khadilkar, M. R.; Al-Dahhan, M.; Duduković, M. P. Parametric Study of Unsteady State Flow Modulation in Trickle Bed Reactors. *Chem. Eng. Sci.* **1999**, *54*, 2585−2595.

(49) Reid, R. C.; Prausnitz, J. M.; Poling, B. *The Properties of Gases and Liquids*; McGraw-Hill: NewYork, 1987.

(50) Wilke, C. R.; Chang, P. Correlation of Diffusion Coefficients in Dilute Solutions. *AICHE J.* **1955**, *1*, 264.

(51) Kern, D. Q. *Process Heat Transfer*; McGraw-Hill: New York 1997.

(52) Dankworth, D. C.; Kevrekidis, I. G.; Sundaresan, S. Time Dependent Hydrodynamics in Multiphase Reactors. *Chem. Eng. Sci.* **1990**, *45*, 2239−2246.

(53) Jiang, Y.; Khadilkar, M. R.; Al-Dahhan, M. H.; Dudukovic, M. P. CFD modeling of multiphase flow in packed bed reactors: I. k-Fluid Modeling Issues. *AIChE J.* **2002**, *48*, 4.

(54) Jiang, Y.; Khadilkar, M. R.; Al-Dahhan, M. H.; Dudukovic, M. P. CFD modeling of multiphase flow in packed bed reactors: II. Results and applications. *AIChE J.* **2002**, *48*, 4.

Received for review August 31, 2004
Revised manuscript received December 13, 2004
Accepted December 15, 2004

IE0402261